PCCP

First-Principles Studies of Polar Perovskite KTaO3 Surfaces: Structural Reconstruction, Charge Compensation, and Stability Diagram

Journal:	*Physical Chemistry Chemical Physics*
Manuscript ID	CP-ART-04-2018-002540.R1
Article Type:	Paper
Date Submitted by the Author:	12-Jun-2018
Complete List of Authors:	Wang, Yaqin; University of Electronic Science and Technology of China, State Key Laboratory of Electronic Thin Films and Integrated Devices Cheng, Jianli; University of California, San Diego, Department of NanoEngineering Behtash, Maziar; University of California, San Diego, Department of NanoEngineering Tang, Wu; University of Electronic Science and Technology of China, State Key Laboratory of Electronic Thin Films and Integrated Devices Luo, Jian; University of California at San Diego, NanoEngineering Yang, Kesong; University of California, San Diego, NanoEngineering Department

Journal Name

ARTICLE TYPE

Cite this: DOI: 10.1039/xxxxxxxxxx

First-Principles Studies of Polar Perovskite $KTaO_3$ Surfaces: Structural Reconstruction, Charge Compensation, and Stability Diagram

Yaqin Wang,[a,b,c] Jianli Cheng,[b] Maziar Behtash,[b] Wu Tang,[c] Jian Luo,[b] and Kesong Yang *[b]

Received Date
Accepted Date

DOI: 10.1039/xxxxxxxxxx

www.rsc.org/journalname

Polar perovskite oxides are of considerable interest for developing advanced functional materials with exceptional electronic properties for their unique polar characters. A cleavage of polar perovskite oxides along the charged layers leads to an electrostatic instability on the cleaved surfaces, and a charge compensation is required to stabilize these surfaces. In this work, we have systemically studied 25 types of surface models of polar $KTaO_3$ perovskite oxide, including (001), (110), and (111) surfaces with various types of surface terminations, using first-principles electronic structure calculations. The surface structural reconstruction, electronic structures, and thermodynamic properties including cleavage energy and surface energy are investigated. The phase stability diagrams of the (001), (110), and (111) surfaces are constructed with respect to the chemical potentials of component elements. The KO (001), O (110), and KO_2 (111) terminations are more likely to be formed than other types of terminations in corresponding surfaces, consistent with experimental observations on $KTaO_3$ (001) surfaces. This work provides useful guidance for accurate control of surface morphology for tailing functional properties of polar $KTaO_3$ perovskite oxide.

1 Introduction

Perovskite oxides with a structural formula ABO_3 exhibit a broad range of attractive physical properties such as ferroelectricity, piezoelectricity, and ferromagnetism for various types of applications.[1–6] A cubic and pseudo-cubic ABO_3 perovskite can be regarded as stacks of alternating AO and BO_2 layers along [001] direction. According to valence states of A and B ions, these perovskite oxides are often classified as polar oxides and nonpolar oxides.[6–11] A nonpolar ABO_3 oxide consists of neutral $(AO)^0$ and $(BO_2)^0$ layers while a polar ABO_3 oxide consists of charged $(AO)^+$ or $(AO)^-$ and $(BO_2)^-$ or $(BO_2)^+$ layers along [001] direction. In recent years, polar perovskite oxides including $A^{3+}B^{3+}O_3$ and $A^+B^{5+}O_3$ have attracted increasing interests due to their unique polar characters that lead to promising applications in energy conversion and nanoelectronics.[8,11–13] For example, La-doped polar perovskite oxide, $NaTaO_3$, with NiO catalyst exhibits a maximum quantum yield of 56% under ultraviolet light (270 nm).[12,14] This can be partially attributed to the high separation rate of electron-hole pairs caused by the built-in electrical field in $NaTaO_3$.

In terms of electron transport property for nanoelectronic application, one remarkable example is the discovery of two-dimensional electron gas (2DEG) at polar/nonpolar $(LaO)^+/(TiO_2)^0$ interface between insulating $LaAlO_3$ and $SrTiO_3$ perovskite oxides in 2004.[7] Since then, a series of extensive studies have been done to explore the formation mechanisms of the interfacial conductivity as well as the related applications.[6,7,9,11] For instance, in addition to the widely studied polar/nonpolar perovskite oxide interfaces,[6,7,15,16] our prior studies also systematically expolore the other two types of interfacial configurations including nonpolar/nonpolar and polar/polar interfaces to create 2DEG at perovskite oxide interfaces, respectively.[9–11,17,18] One model system to produce 2DEG based on polar/polar perovskite oxide interface is $LaAlO_3/KTaO_3$.[11] Our first-principles computational studies show that the 2DEG can be formed at polar/polar $(LaO)^{+1}/(BO_2)^{+1}$ (B=Nb and Ta) interface for $LaAlO_3/A^+B^{5+}O_3$ (A = Na and K, B = Nb and Ta) heterostructures. In addition to the interfacial conductivity, polar perovskites also show impressive surface electronic properties. For example, a 2DEG has been observed on the non-reconstructed quasi-planar (001) and (111) polar surfaces of $KTaO_3$ using angle-resolved photoemission spec-

[a] Department of Material Science and Engineering, Xihua University, Chengdu, 610039, P. R. China.
[b] Department of NanoEngineering, University of California, San Diego, La Jolla, CA 92093-0448, USA.
[c] State Key Laboratory of Electronic Thin Films and Integrated Devices, University of Electronic Science and Technology of China, Chengdu 610054, P.R.China.
* Fax: +1-858-534-9553; Tel: +1-858-534-2514; E-mail: kesong@ucsd.edu

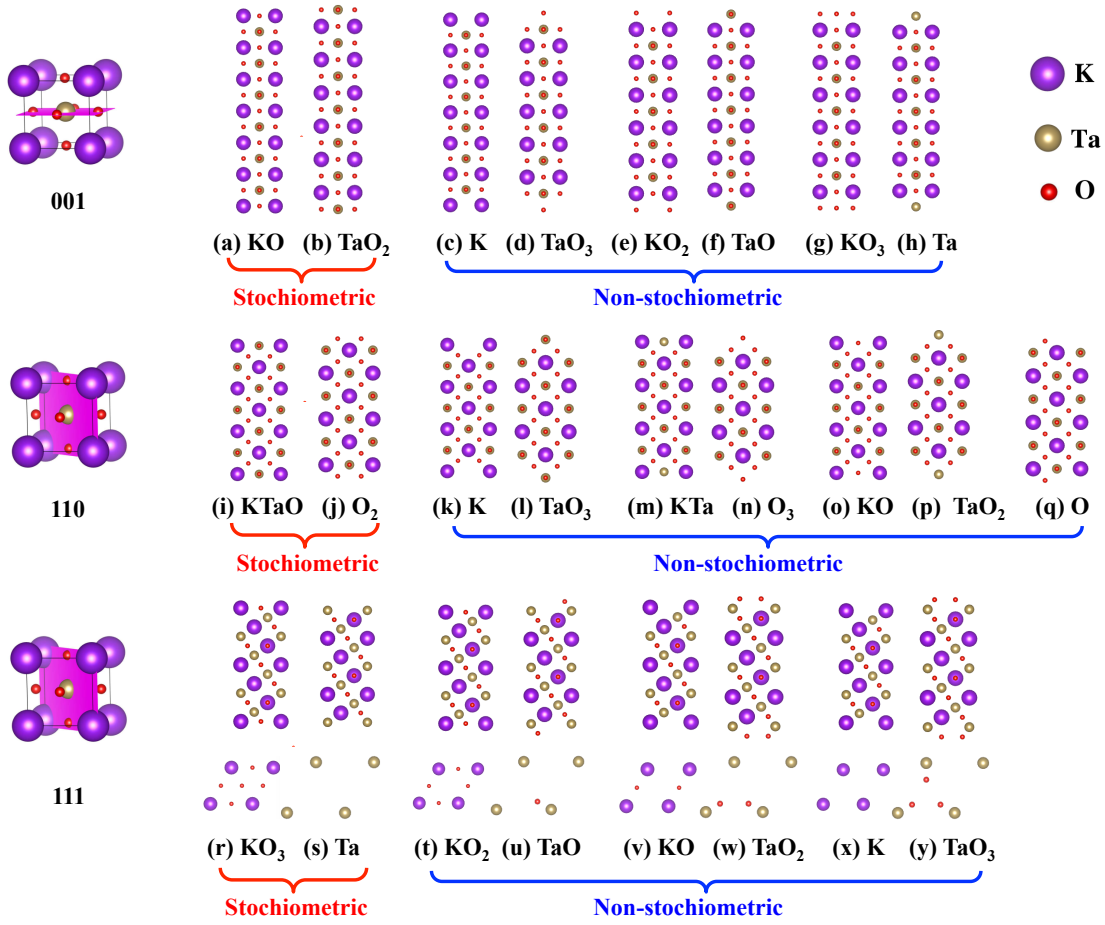

Fig. 1 (Color online) 25 slab models of $KTaO_3$ (001), (110) and (111) surfaces. (a, b) Stochiometric and (c-h) non-stochiometric $KTaO_3$ (001) surface models; (i, j) stochiometric and (k-q) non-stochiometric $KTaO_3$ (110) surface models; (r, s) stochiometric and (t-y) non-stochiometric $KTaO_3$ (111) surface models. Note that the $KTaO_3$) (110) surface with O termination (q) is symmetrical to its complementary surface model and thus only one surface is shown. For $KTaO_3$ (111) models, their side and top views are plotted to clearly show their surface structures.

troscopy in the experiment.[19–21] $KTaO_3$ (001) surface has been found to have superconductivity upon electrostatic carrier doping.[22] The (001) surface also shows large Rashba effects due to the strong spin-orbit coupling interactions.[23–25]

In spite of the remarkable electronic properties and promising applications of the polar perovskite oxides, the charged layers of polar perovskite oxides determine that their surfaces such as (001), (110) and (111) surfaces bear a nonzero dipole moment and thus exhibit an electrostatic instability. Although the instability might be compensated by charge redistribution in the outer surface layers, surface structural reconstructions, and chemical doping,[8,26] the surface properties will be modified accordingly. Let us take polar $KTaO_3$ as an example. A vacuum-cleaved (001) $KTaO_3$ surface has been observed to show a 2DEG.[20] However, later experiments show that (001) $KTaO_3$ surface can be metallic only after Ar^+ irradiation in vacuum and the metallic state will disappear upon annealing in oxygen at 300 °C.[27,28] These observations imply that the polar (001) $KaTaO_3$ surface undergoes a structural reconstruction, which modifies surface electronic property accordingly.[29] Therefore, a comprehensive understanding of the surface structural reconstruction and thermodynamic property of the polar perovskite oxides is very essential to control their surface morphology for tailoring functional properties.

In this work, by using first-principles electronic structure calculations, we modeled the 25 surface models of polar $KTaO_3$ perovskite including (001), (110), and (111) polar surfaces with various surface terminations, and systemically studied their surface structural reconstruction, charge compensation mechanism, and surface thermodynamic properties. The phase stability diagrams of the considered surfaces were also constructed with respect to the chemical potentials of component elements.

2 Computational and structural details

In this work, all the density functional theory (DFT) calculations were performed using Vienna *Ab-initio* Simulation Package (VASP).[30,31] The projector augmented-wave (PAW) potentials were applied for electron-ion interactions.[32] The generalized gradient approximation (GGA) parameterized by Perdew-Burke-Ernzerhof (PBE) was employed for exchange-correlation functional.[33] A cutoff energy of 450 eV was used for the plane-wave basis set to converge the total energy. The *k*-space grids of $6\times6\times6$ and $4\times4\times1$ within Monkhorst-Pack scheme were employed to sample the Brillouin zone of the bulk and slab models, respectively. All the atomic positions were optimized until the

Table 1 Atomic relaxations (in Å) along *z*-axis for the (001) configurations of $KTaO_3$ surface.

Terminations		Stochimetric		Non-stochiometric					
		KO	TaO_2	K	TaO_3	KO_2	TaO	KO_3	Ta
L1	K	-0.30		-0.41					
	Ta		0.00				-0.10		-0.16
	O	-0.09	-0.25		-0.17	-0.68	-0.42	-1.24	
L2	K		-0.08			-0.99	-0.07	-1.22	-0.09
	Ta	-0.26		-0.01	-0.39				
	O	-0.09	-0.17	-0.30	-0.13	-0.08	-0.31	-0.09	-0.39
L3	K	-0.13		0.01	-0.22				
	Ta		0.04			-0.27	0.04	-0.29	0.03
	O	0.00	-0.11	-0.18	-0.01	-0.05	-0.16	-0.06	-0.18
L4	K		0.00			-0.14	0.02	-0.15	0.01
	Ta	-0.12		0.06	-0.14				
	O	-0.01	-0.07	-0.09	-0.02	0.02	-0.11	0.02	-0.12
L5	K	-0.05		0.02	-0.06				0.05
	Ta		0.04			-0.08	0.05	-0.08	
	O	0.02	-0.04	-0.06	0.02	0	-0.05	0	-0.06
L6	K		0.01	0.03		-0.02	0.01	-0.02	0.01
	Ta	-0.04			-0.04				
	O	0.00	-0.02	-0.02	0	0.01	-0.03	0.01	-0.03

Table 2 Atomic relaxations (in Å) along *z*-axis for the (110) configurations of $KTaO_3$ surface. Note that if there are more than two O ions in the same layer, after structural relaxation, the O ions may exhibit different degrees of displacement, and their atomic relaxations are listed in the parentheses.

Terminations		Stochimetric		Non-stochiometric						
		KTaO	O_2	K	TaO_3	KTa	O_3	KO	TaO_2	O
L1	K	-0.35		0.14		-0.69		-0.36		
	Ta	0.20			0.17	0.20			0.17	
	O	-0.08	-0.03		-0.28		0.47	-0.8		0.07
L2	K		-1.99							-0.80
	Ta		-0.16							0.14
	O	-0.21	0.07	-0.05	-0.11	-0.23	0	-0.05	-0.16	0.04
L3	K	0.09		-0.25	0.09	0.10	0.05	-0.75	0.09	
	Ta	0.06		-0.08	0.06	0.06	-0.24	-0.11	0.06	
	O	-0.07	0.04	0.07	-0.05	-0.08	-0.08	0.07	-0.06	0.12(-0.18)
L4	K		-0.05							0.06
	Ta		-0.13							-0.01
	O	-0.08	0.04	0.02	-0.06	-0.09	0.01	0.02	-0.07	0.04
L5	K	0.03		-0.02	0.03	0.03	-0.05	-0.02	0.03	
	Ta	0.05		-0.05	0.04	0.05	-0.06	-0.08	0.05	
	O	-0.02	0.02	0.03	-0.02	-0.03	0.04	0.04	-0.02	0.03(-0.09)
L6	K		-0.02							0.00
	Ta		-0.03							0.00
	O	-0.02	0.01	0.01	-0.02	-0.02	0	0.01	-0.02	0.00

interatomic forces were smaller than 0.03 eV/Å. The electronic self-consistency calculation was assumed for a total energy convergence of less than 10^{-5} eV. A Bader charge analysis was employed to analyze charge distribution.[34,35]

$KTaO_3$ crystallizes in a cubic phase with space no. 221 ($Pm\bar{3}m$) at room temperature.[36,37] Its surface models were built using optimized bulk lattice constant a = 4.028 nm. These surface models can be classified as two classes, *i.e.*, stoichiometric and non-stochiometric, according to surface terminations. Herein, stoichiometric means that the surface termination has the same atomic composition ratio with that of the corresponding layer in the bulk compound, and the stoichiometric terminations can be created by directly cleaving the bulk structure along a specific plane. That is, we have a total number of six stoichiometric surface models for three surface planes: KO and TaO_2 in the (001) surface plane, KTaO and O_2 in the (110) surface plane, and KO_3 and Ta in the (111) surface plane. The non-stoichiometric terminations can be formed via adsorption or desorption of one or more atoms on the stoichiometric surfaces. Specifically, non-stochiometric surface terminations of $KTaO_3$ can be artificially made by removing or adding O (K) atoms. In this work, we modeled nineteen non-stochiometric surface terminations including six on the (001) surface (K-, TaO_3-, KO_2-, TaO, KO_3-, Ta-terminated surfaces), seven on the (110) surface (K-, TaO_3-, KTa-, O_3-, KO-, TaO_2-, and O-terminated surfaces), and six on the (111) surface (KO_2-, TaO-, KO-,TaO_2, K-, and TaO_3-terminated surfaces). The geometrical structures of these 25 total surface models including six stoichiometric and nineteen non-stoichiometric are shown in Fig. 1. A slab approach with two symmetrical surfaces was used in our work to model these surface structures, with each having a thickness of 13 layers (6.5 unit cells). To avoid the dipole-dipole interaction between two periodic images,[38] a vacuum layer with a thickness of 20 Å was added in the slabs.

Table 3 Atomic relaxations (in Å) along *z*-axis for the (111) configurations of $KTaO_3$ surface.

Terminations		Stochimetric		Non-stochiometric					
		KO_3	Ta	KO_2	TaO	KO	TaO_2	K	TaO_3
L1	K	-0.64		-0.46		-0.41		-0.48	
	Ta		0.44		0.27		0.17		0.09
	O	-0.02		-0.01	-0.32	-0.49	-0.12		-0.35(0.86)
L2	K		-0.25		-0.24		-2.93		-2.98
	Ta	-0.14		0.08		0.17		0.30	
	O		-0.21		-0.12(-0.07)		0.09(-0.15)		0.03
L3	K	-0.20		-0.15		0.09		0.01	
	Ta		0.06		0.06		-0.07		0.07
	O	0.04		-0.02(0.04)		-0.26(-0.21)		-0.23	
L4	K		0.16		0.08		0.01		0.03
	Ta	-0.08		0.00		0.05		0.06	
	O		-0.09		-0.06(-0.03)		0.04(0.02)		0.02(0.03)
L5	K	-0.02		0.03		0.11		0.13	
	Ta		0.03		0.02		-0.13		-0.01
	O	0.02		-0.05(0.02)		-0.08		-0.08	
L6	K		0.03		0.01		-0.03		0
	Ta	-0.03		-0.01		0.02		0.02	
	O		-0.02		-0.02(-0.01)		0.02(0.00)		-0.01

3 Results and discussion

3.1 Surface Relaxations

We began by studying structural reconstruction of $KTaO_3$ surface models. It is expected that structural relaxation can significantly modify the materials properties of the surfaces. For instance, a prior work showed that a structural reconstruction of $KTaO_3$ (001) surface could screen out the polar field and suppress the spin-splitting effect.[20,23] Hence, it is quite necessary to study the structural relaxations of these surface models. The results of structural changes caused by relaxation are summarized in Tables 1-3. Only the data of the six outermost layers are presented since all the slab models are symmetric. The positive (negative) values in the table indicate that the atoms move inward (outward) the center of the slab models. Our calculations show that the relaxations mainly occur in the five outermost layers for all the terminations, and the largest relaxation occurs in the first three layers. To clearly show the structural reconstruction, the unrelaxed and relaxed surface models are plotted in Fig. S1-S3 of the Supporting Information.

For the (001) surface, there are a total number of eight possible surface terminations, and the noticeable atomic relaxations occur at their first three layers, see Table 1. For instance, for the KO- and K-terminated models, the large relaxation occurs in the surface layer, with K atoms moving outward by 0.30 Å, and 0.41 Å, respectively; for the TaO_2- and TaO-terminated surfaces, the surface O atoms show the largest displacement with -0.25 Å, and -0.42 Å, respectively; for KO_2 and KO_3 terminations, all the atoms in the first two layers present largest displacement, with the K atom moving outward by 0.99 Å, and 1.22 Å, respectively; for TaO_3 and Ta terminations, the largest relaxation occurs in the second layer where Ta or O atom moves outward by 0.39 Å.

For KTaO termination in the (110) surface, as shown in Table 2, K atoms in the first layer move outward by 0.35 Å, while those in other layers move toward the center of the slab model and magnitude of the displacement of these K atoms decrease from the surface to the center of the slab model, reaching about 0.03 Å in the fifth layer. For K, TaO_3, and TaO_2 terminations, all the atoms show a relatively small displacement. For TaO_3 and TaO_2 terminations, the largest relaxation occurs in the first layer where Ta atom both moves inward by 0.17 Å. For K termination, in contrast, the largest relaxation occurs in the third layer, about -0.25 Å. For KTa, O_3, and KO terminations, atomic relaxations mainly occur in the first three layers, with a relatively large displacement. For O_2 (110) and O (110) terminations, K atoms in the second layer move outward the surface. This different displacement behavior of Ta and K atoms can be explained from a perspective of a large charge disparity between Ta and K. This determines that Ta atoms tend to descend into the bulk, while K atoms tend to migrate to the surface.[29]

For the (111) surface, all the surface termination models show a large displacement in the topmost layers, and this displacement rapidly decreases as the layer number increases, *i.e.*, from the topmost surface layer to inner layers, see Table 3. For KO_3, KO_2, and K terminations, the atom displacement mainly occurs in the first layer, with the K atom moving outward by 0.64 Å, 0.46 Å, and 0.48 Å, respectively. For KO termination, K and O atoms both move outward from the center of the slab to the first layer. For Ta and TaO terminations, structural relaxations mainly occur in the top two layers with Ta atoms moving inward and K and O atoms moving outward. For TaO_2 and TaO_3 terminations, K atoms in the second layer move to the topmost surface layer, similar to the case of O_2 and O terminations in the (110) surface, showing a moving tendency of K atoms to the surface.

3.2 Charge Compensation and Electronic Structures

Next we studied the surface charge compensation and surface electronic structures by analyzing the surface Bader charge and density of states (DOS), respectively. It is known that an ideal polar surface is not stable because of surface dipole moment.[39] To stabilize these polar surfaces, the surface dipole moment needs to be removed or canceled out by compensating charge density of outer layers of the slab. For cubic perovskites such as $KTaO_3$, the condition of canceling out the macroscopic dipole moment can be

described using following equation:[26,40,41]

$$\sum_{j=1}^{m} \sigma_j = -\frac{\sigma_{m+1}}{2} \quad (1)$$

where m is the number of modified outer layers, σ_j and σ_{m+1} represent the charge of the layers j and $m+1$, respectively. For $KTaO_3$, as discussed below, to cancel out the surface dipole moment and to stabilize the surface, the charge of all the six outer layers needs to be redistributed. In other words, at $m=6$, the total charge of the six outer layers is half value of the seventh layer. In fact, the charge distribution of the seventh layer is very close to that in the bulk layer.

To evaluate the surface charge distribution, we calculated the layer-resolved Bader charges for the three types of surfaces with both stoichiometric and non-stoichiometric terminations. Considering the symmetry of slab models, only the Bader charge of seven outermost layers are calculated, see Tables SI-SIII of the Supporting Information. For a comparison, we also calculated the Bader charge of bulk $KTaO_3$, that is, 0.8, 2.8, and -1.2 for K, Ta, and O atoms, respectively. Accordingly, the total Bader charge is -0.4 (0.4) for KO (TaO_2) termination layer of (001) surface, 2.4 (-2.4) for KTaO (O_2) termination layer of (110) surface, and -2.8 (2.8) for KO_3 (Ta) termination layer of (111) surface, respectively. For the KO-terminated (001) surface, the calculated total Bader charge of the six outer layers ($\sum_{l=1}^{6} \sigma$) is about 0.17 and that of the seventh layer σ_7 is about -0.33. For the TaO_2-terminated (001) surface, $\sum_{l=1}^{6} \sigma = -0.16$ and $\sigma_7 = 0.33$. Similarly, for (110) and (111) surfaces, they all follow the relationship, $\sum_{l=1}^{6} \sigma = -1/2\sigma_7$. It is noted that the seventh layer is relatively far away from the surface, and thus its layer charges are similar to those in the bulk $KTaO_3$. In short, our calculations confirm that the equation 1 can be fully satisfied. The charge distribution mechanism for these 25 surface models can also be analyzed from their DOS, which is discussed from the types of surface terminations as below, *i.e.*, stoichiometric and non-stoichiometric.

3.2.1 Stoichiometric Terminations

There are six stoichiometric terminations, *i.e.*, KO- and TaO_2-terminated (001) surfaces, KTaO- and O_2-terminated (110) surfaces, and KO_3- and Ta-terminated (111) surfaces. The stoichiometry of these surface layers is same with their corresponding bulk layers of $KTaO_3$, and thus it is expected that the charge distribution can be achieved only by modifying electron occupations of surface states. On the basis of the condition of canceling out the surface dipole moment, *i.e.*, equation 1, the total charge of outermost surface layer should be equal to half value of the charge in their corresponding bulk layers. Let us take KO- and TaO_2-terminated (001) surfaces as an example to analyze its surface charge redistribution from viewpoints of surface electronic structures. Note that the charge of bulk KO layer is $-1e$ and that of the TaO_2 layer is $+1e$. Therefore, to satisfy equation 1, after charge redistribution, the surface charge of KO layer should be close to $-0.5e$, implying that surface O atoms capture 0.5 e less electrons than the bulk O atoms and thus O 2p orbitals should be not fully occupied. For surface TaO_2 layer, its surface charge should be close to $+0.5e$, indicating that the surface Ta atoms lose 0.5e less electrons than the bulk Ta atoms and thus Ta 5d orbitals should be partially occupied. To verify this hypothesis, we calculated the total DOS for the six stoichiometric surface terminations and the partial DOS for the atoms in the outermost layer, see Fig. 2. The total and partial DOS of the bulk $KTaO_3$ are also calculated as a comparison. For KO (001) surface termination, the Fermi level crosses the valence band (VB) and some O 2p orbitals are unoccupied, showing a p-type-like conductivity, while for TaO_2 (001), Fermi level is pinned just above the bottom conduction band (CB) and some Ta 5d orbitals are occupied, showing an n-type conductivity. These results show that the calculated DOS is well consistent with our surface charge redistribution analysis. Similar charge redistribution can be also applied on the O_2 and KTaO (110) surface terminations, and KO_3 and Ta (111) surface terminations, which can also be verified from their surface electronic structures, see Fig. 2(c-f).

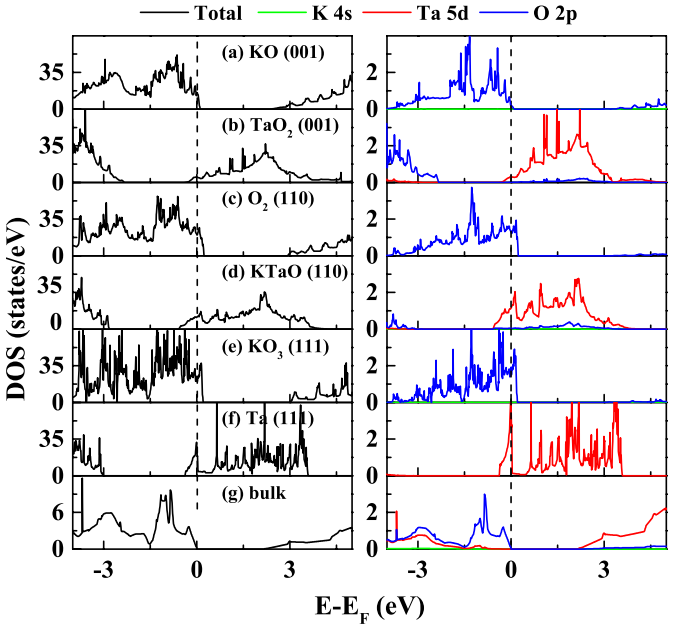

Fig. 2 (Color online) Calculated total DOS and partial DOS of the (a) KO (001), (b) TaO_2 (001), (c) O_2 (110), (d) KTaO (110), (e) KO_3 (111), and (f) Ta (111) terminations compared with the bulk material. Note that the partial DOS is calculated for the outermost layers only.

3.2.2 non-stoichiometric Terminations

Here we studied nineteen non-stoichiometric surface models including K, TaO_3, KO_2, TaO, KO_3, and Ta (001) surface terminations, K, TaO_3, KTa O_3, KO, TaO_2, and O (110) surface terminations and KO_2, TaO, KO, TaO_2, K, and TaO_3 (111) surface terminations. These non-stoichiometric surface terminations can be obtained from a modification of a stoichiometric surface by adsorbing or desorbing its constituting atoms. The bulk $KTaO_3$ consists of alternative stoichiometric $(KO)^{-1}$ and $(TaO_2)^{+1}$ layers along [001] direction. To satisfy equation 1, the charges of these outermost non-stoichiometric (001) surface layers should be close to half value of those in their corresponding bulk layers,

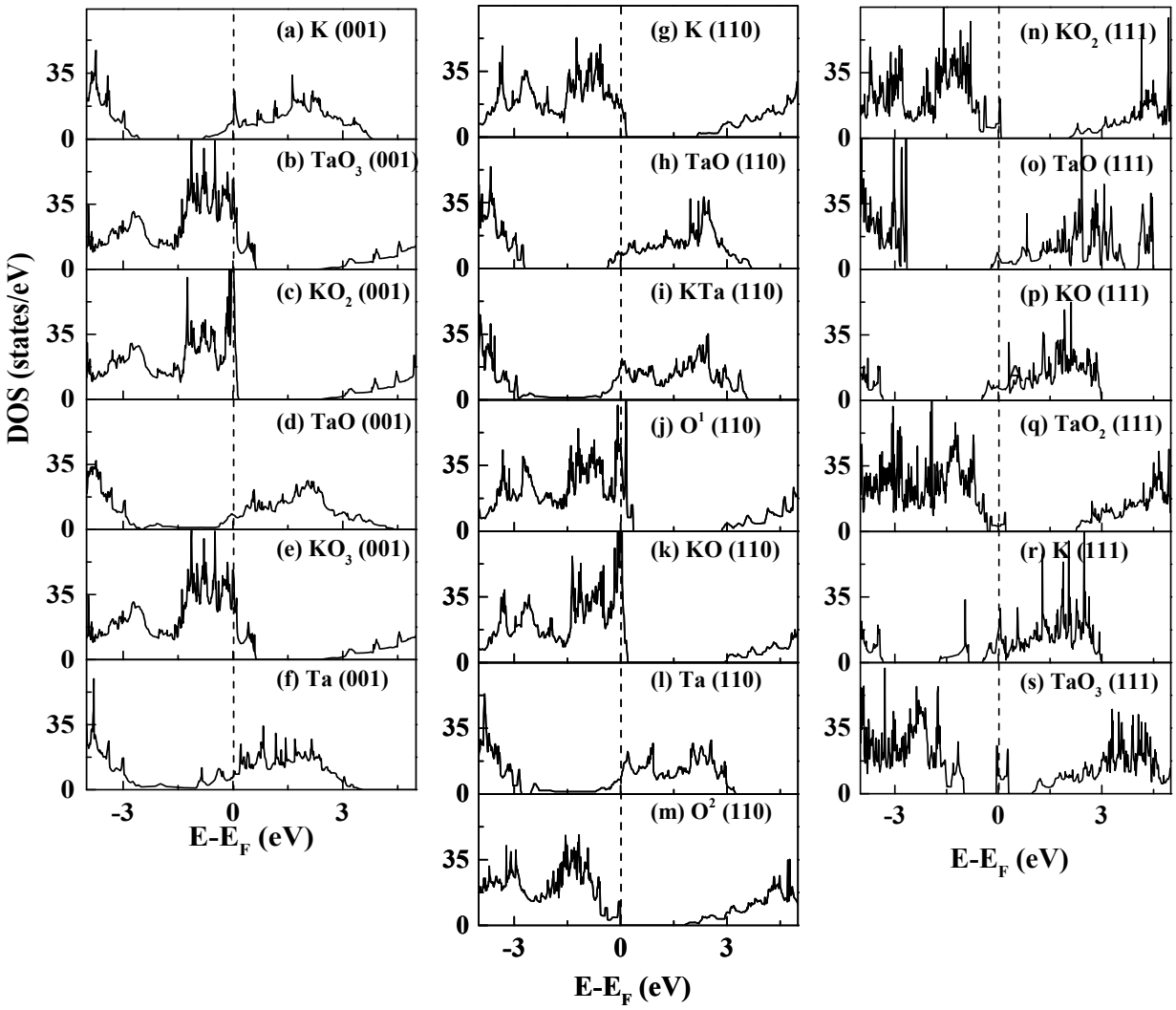

Fig. 3 (Color online) Calculated total DOS for all the non-stoichiometric terminations. The most left column is for $KTaO_3$ (001) surface, the middle one is for $KTaO_3$ (110) surface, and the most right one is for $KTaO_3$ (111) surface.

i.e., $(KO)^{-1}$ and $(TaO_2)^{+1}$ layers. In other words, the K, KO_2, and KO_3-terminated (001) surfaces should have a charge close to $-0.5e$, while the TaO_3, TaO, and Ta-terminated (001) surfaces close to $0.5e$. However, the K, KO_2, KO_3, TaO_3, TaO, and Ta layers have a formal charge of $1e$, $-3e$, $-5e$, $-1e$, $3e$, $5e$ to their ionic limit, respectively. This implies that the TaO_3, KO_2, and KO_3-terminated (001) surface must donate $1.5e$, $2.5e$, and $4.5e$, respectively, and their total DOS will exhibit a *p*-type-like character. In contrast, the K, TaO, Ta-terminated (001) surface should accept $1.5e$, $2.5e$, and $4.5e$, respectively, and their total DOS will show a *n*-type behavior. To further verify this hypothesis, we calculated total DOS for K, TaO_3, KO_2, TaO, KO_3 and Ta-terminated (001) surfaces, see Fig. 3(a-f), which is in an excellent agreement with above analysis of the charge distribution.

A similar analysis can also be applied on the (110) and (111) surfaces. The bulk $KTaO_3$ consists of alternative stoichiometric $(KTaO)^{+4}$ and O_2^{-4} layers along [110] direction. The K, KTa, KO-terminated surfaces have a charge of $1e$, $6e$, $-1e$, as compared to the half values ($2e$) from their corresponding bulk layers $(KTaO)^{+4}$, respectively. This indicates that K and KO-terminated surface should lose about $1e$ and $3e$, respectively. Then their total DOS should exhibit a *p*-type-like character, see Fig.3g and 3k. While KTa-terminated surface should accept about $4e$ to meet equation 1, and its total DOS should show a *n*-type behavior, see Fig.3i. Similarly, the TaO_3, O_3, and TaO_2-terminated surfaces should have a charge close to $-2e$. The Fermi levels of TaO_2- and TaO_3-terminated are pinned above the conduction band bottom, presenting a *n*-type behavior. While in O_3-terminated surface, the Fermi level just below the valence band maximum. As a comparison, interestingly, the O-terminated (110) surface have a charge of $-2e$, which is half value of the bulk O_2^{-4} layer, indicating that the O-terminated (110) surface does not need donate or accept any electrons. This means that the total DOS of O-terminated (110) surface should exhibit a typical insulating behavior.

The bulk $KTaO_3$ consists of alternative stoichiometric $(KO_3)^{-5}$ and Ta^{+5} layers along [111] direction. The KO_2- and TaO-terminated surfaces have a charge of $-3e$ and $3e$, as compared to the half values ($-2.5e$ and $2.5e$) of the charges of their corresponding bulk layers, respectively. This indicates that KO_2-terminated surface should lose about $0.5e$ while TaO-terminated surface should donate about $0.5e$ to meet equation 1, and thus their total DOS should exhibit a *p*-type and *n*-type character, respectively, as shown in Fig. 3n and 3o. Similarly, KO, TaO_2, K- and TaO_3-terminated (111) surfaces have a charge of $-e$, e, e, and $-e$. To satisfy equation 1, the KO and K-terminated surface need to accept additional $1.5e$ and $3.5e$, while TaO_2 and TaO_3-terminated surface need to donate around $1.5e$ and $3.5e$, respectively. As shown in Fig. 3(p-s), the Fermi levels in the KO- and K -terminated surfaces are pinned just above the conduction band bottom, while in TaO_2 and TaO_3 just below the valence band maximum, respectively, which is well consistent with our charge redistribution analysis.

3.3 Thermodynamic Stability

The relative thermodynamic stability of these different surface terminations is highly dependent on the energetic consideration. In this section, we introduce three physical quantities to analyze the thermodynamic stability, *i.e.*, cleavage energy E_{cleav}, surface energy E_s, and surface grand potential Ω_i.

3.3.1 Cleavage Energy

The cleavage energy is conventionally defined as the energy per unit area required to separate a crystal into parts and thus to form complementary stoichiometric surface terminations. It is an effective parameter to judge whether a stoichiometric surface termination is relatively easy to form. The cleavage energy of a relaxed surface can be calculated using below equation:[42]

$$E_{cleav} = \frac{1}{2S}[E^{rel}_{slab}(A) + E^{rel}_{slab}(B) - nE^{bulk}_{KTaO_3}] \quad (2)$$

where $E^{rel}_{slab}(A)$ and $E^{rel}_{slab}(B)$ are the total energy of the symmetric slab with the *A* and *B* surface terminations, respectively. *A* and *B* denote two complementary terminations. *S* is the surface area of the cleavage plane. $E^{bulk}_{KTaO_3}$ refers to the total energy of bulk $KTaO_3$ unit cell. *n* is the total number of the bulk $KTaO_3$ unit cell in the two slabs. There are three groups of complementary and stoichiometric surface terminations, including KO and TaO_2 in the (001) plane, KTaO and O_2 in the (110) plane, and KO_3 and Ta in the (111) plane, respectively. The calculated cleavage energies of these surface terminations are listed in Table 4. To have a comparison, cleavage energies of several other perovskite oxides are also listed.[43–47] Our calculations show that KO/TaO_2 (001) plane has the lowest cleavage energy, while the stoichiometric KO_3/Ta (111) plane has the highest one. This finding is similar to the case in the $LaAlO_3$,[43] $SrZrO_3$[44] and $ATiO_3$ (A=Sr, Ba, and Pb).[45–47]

Table 4 Comparison of the cleavage energies for the (001), (110), and (111) stoichiometric terminations of $KTaO_3$ surfaces.

Term.	(001)	(110)	(111)
	KO/TaO_2	KTaO/O_2	KO_3/Ta
E_{cleav}(J/m^2)	2.43	6.40	6.78
$LaAlO_3$ [43]	1.54	4.27	
$SrZrO_3$ [44]		2.81	
$BaZrO_3$ [48]	1.17	3.87	
$SrTiO_3$ [45]		6.52	
$BaTiO_3$ [47]		2.90	
$PbTiO_3$ [46]		2.46	

3.3.2 Surface Energy

In thermodynamics, the surface energy is defined as:

$$\gamma = (\frac{\partial G}{\partial A_{surf}})_{T,P,N_j} = (\frac{\partial \Omega}{\partial A_{surf}})_{T,V,\mu_j} \quad (3)$$

where Ω is the surface grand potential, also known as the Landau free energy. A_{surf} is total surface area ($2S$ in our simulation). For a multi-component system with surface adsorption, whose surface composition or stoichiometry is different from that in the abutting bulk phase, the second definition at constant chemical potentials in an open system is practically more useful. One can find the equilibrium surface energy and the associated equilibrium surface configuration via minimizing the surface excess of grand potential at constant chemical potentials and other thermodynamic state variables:

$$\gamma_{eq.} = min(\frac{\Omega^{xs}}{A_{surf}})_{T,\mu_j} \quad (4)$$

$$\frac{\Omega^{xs}}{A_{surf}} = \frac{E^{xs}}{A_{surf}} - T\frac{S^{xs}}{A_{surf}} - \sum_j \mu_j \Gamma_j \quad (5)$$

where $\frac{E^{xs}}{A_{surf}}$, $\frac{S^{xs}}{A_{surf}}$, and Γ_j, respectively, are the surface excess of internal energy, entropy, and the amount of the *j-th* component (surface adsorption amount) per unit area in the Gibbs dividing plane approach. Noting that the specific values of E^{xs}, S^{xs}, and Γ_j depend on the selection of the Gibbs dividing plane, but the equilibrium surface energy $\gamma_{eq.}$ is a physical property of the surface that depends only on thermodynamic state variables such as chemical potentials, temperature and pressure. It is worth emphasizing that, $\gamma_{eq.}$ in equation 4 refers to the equilibrium surface energy that corresponds to the lowest excess grand potential at given chemical potentials and other thermodynamic state variables.

An estimation of the surface energy can be obtained by using the unrelaxed cleavage energy and by conducting additional structural relaxation calculations. This approach is often used as a first-order approximation of the surface energy. Specially, for a cleavage that form a pair of complementary terminations A and B at $T = 0$, we can estimate:

$$\gamma_0 \approx \frac{\frac{1}{2}[\Omega^{xs}(A) + \Omega^{xs}(B)]}{2S} = \frac{\frac{1}{2}[E^{xs}(A) + E^{xs}(B)]}{2S}$$
$$= \frac{1}{2}[E^{unrel}_{cleav} + E_{rel}(A) + E_{rel}(B)] \quad (6)$$

Table 5 Comparison of the surface energies for the (001), (110), and (111) stoichiometric terminations of $KTaO_3$ surfaces.

Term.	(001)		(110)		(111)	
	KO	TaO_2	KTaO	O_2	KO_3	Ta
E_s(J/m^2)	1.36	1.08	3.23	3.17	3.77	3.01
$SrTiO_3$ [49]	0.98	0.97	4.37	4.21	5.52	4.26
$SrZrO_3$ [50]	1.13	1.24		2.21		
$PbZrO_3$ [50]	1.00	0.93		1.74		

with

$$E_{rel}(A) = \frac{1}{2S}[E^{rel}_{slab}(A) - E^{unrel}_{slab}(A)] \quad (7)$$

$$E_{rel}(B) = \frac{1}{2S}[E^{rel}_{slab}(B) - E^{unrel}_{slab}(B)] \quad (8)$$

where $E^{unrel}_{slab}(A)$ $[E^{unrel}_{slab}(B)]$ and $E^{rel}_{slab}(A)$ $[E^{rel}_{slab}(B)]$ are the total energy of the unrelaxed and relaxed symmetric slabs with the *A (B)* surface termination,respectively. Noting that terminations A and B are a complementary pair so that the term $\sum_j \mu_j \Gamma_j$ cancels each other in the averaging in equation 6. Also, the subscript 0 in equation 6 denotes that this estimation represents the case with average $\Gamma_j = 0$ (as well as T = 0).

In practical calculations, it is common to separate γ_0 into two parts for two complementary terminations (after cleavage):

$$\gamma_0 = \frac{1}{2}[E_s(A) + E_s(B)] \quad (9)$$

with

$$E_s(A) = \frac{1}{2}E^{unrel}_{cleav}(A) + E_{rel}(A) \quad (10)$$

$$E_s(B) = \frac{1}{2}E^{unrel}_{cleav}(B) + E_{rel}(B) \quad (11)$$

in which $E_s(A)$ and $E_s(B)$ are the surface energies of A-terminated and B-terminated surfaces, respectively. This method is very convenient but somewhat arbitrary. By following this approach, the calculated surface energies for the (001), (110), and (111) stoichiometric terminations of $KTaO_3$ surfaces are summarized in Table 5, along with the values for other perovskite oxides $SrTiO_3$, $SrZrO_3$, and $PbZrO_3$.[49,50] Our calculations show that the (001) surfaces have lower surface energies than the (110) and (111) surfaces, which is consistent with the case in $SrTiO_3$,[49] $SrZrO_3$, and $PbZrO_3$ systems.[50]

It is important to note that even at T = 0 K, the $E_s(A)$ and $E_s(B)$ defined above are neither γ (the rigorously-defined surface energy) nor the $\frac{E^{xs}}{A_{surf}}$ (the Gibbs excess quantity that depends on the selection of Gibbs diving plane), though they are still often called “surface energy" in literature. A more rigorously defined surface energy in equations 3-5 will be discussed in more details in the next section.

3.3.3 Surface Stability Diagram

The fundamental thermodynamic principles tell us that the equilibrium surface configuration is dictated by the state that has minimum surface energy (also called excess surface grand potential) with constant chemical potentials as defined in equations 3-5. A thermodynamic state of such a surface (or interface in general) is essentially a 2-D interfacial phase (which is also called a “complexion" to differentiate them from the bulk phase defined by Gibbs).[51,52] First-order or continuous phase-like transitions between different surface complexions (2-D interfacial phases) can occur when a thermodynamic state variable is varied. Thus, we can construct surface stability phase diagram to represent the relative stabilities of different surface phases/complexions as well as the boundaries that represent surface phase-like transitions. Such stability (interfacial phase) diagrams have been constructed for oxide surfaces by both experiments and modeling,[47,49,50] as well as for hetero-phase interfaces[53] and grain boundaries[54–61] via different methods.

To construct a surface stability phase diagram, one should compute the surface energies for different surface configurations (complexions) as functions of thermodynamic state variables such as chemical potentials (as well as temperature and pressure in some other studies). The surface configuration that has the lowest surface excess of grand potential (according to equation 5) represents the stable equilibrium surface phase/complexion. Its surface excess of grand potential dictates the equilibrium surface energy (γ_{eq}) according to equation 4. Then, one can map out the surface stability diagram, which is essentially a surface phase diagram. Note that this study is limited to calculating different perfect (1×1) terminations at T = 0, while reconstruction and formation of vacancies and disordering at high temperatures will be considered in future studies.

Specifically, we calculated the surface stability diagram for the (001), (110), and (111) surfaces of $KTaO_3$ by using the surface excess grand potential approach. Since $\Omega^{homo} = E - TS - \sum_j \mu_j N_j = -PV$ for a homogeneous system without surface (noting that $\sum_j \mu_j N_j = G = E + PV - TS$), the total grand potential for a system with surfaces (our calculation slab of the $KTaO_3$ system with two symmetrical surfaces of termination *i*) is:

$$\begin{aligned}\Omega^{total}_i &= E^i_{slab} + PV - TS - N_K\mu_K - N_{Ta}\mu_{Ta} - N_O\mu_O \\ &= \Omega^{homo} + \Omega^{xs}_i = -PV + \Omega^{xs}_i\end{aligned} \quad (12)$$

where E^i_{slab} is the total energy of the slab system. N_K, N_{Ta}, and N_O are the number of K, Ta, and O atoms in the slab model, respectively. μ_K, μ_{Ta}, and μ_O represents the chemical potentials of the K, Ta, and O atoms, respectively. Thus, the surface excess grand potential per unit area (or surface energy) of the *i* termination can be calculated using the below formula[62]

$$\omega_i = \frac{\Omega^{xs}_i}{2S} = \frac{1}{2S}[E^i_{slab} + PV - TS - N_K\mu_K - N_{Ta}\mu_{Ta} - N_O\mu_O] \quad (13)$$

where 2*S* is the total surface area. Note that the factor of 1/2 corresponds to two symmetric surfaces in the slab model. For a solid material, *PV* term is a constant and small in our calculations at 0 K and a sufficient low temperature, then the entropic contribution is negligible and the *PV* and *TS* terms can be neglected and the above formula can be rewritten as[45]

$$\omega_i = \frac{\Omega^{xs}_i}{2S} \approx \frac{1}{2S}[E^i_{slab} - N_K\mu_K - N_{Ta}\mu_{Ta} - N_O\mu_O] \quad (14)$$

The chemical potential of the relevant atoms are linked by the thermodynamic stability of the $KTaO_3$ phase, *i.e.*,

$$\mu_{KTaO_3} = E^{bulk}_{KTaO_3} = \mu_K + \mu_{Ta} + 3\mu_O. \quad (15)$$

We then introduced the following chemical potentials for each atomic specie:

$$\Delta\mu_K = \mu_K - E^{bulk}_K \quad (16)$$

$$\Delta\mu_{Ta} = \mu_{Ta} - E^{bulk}_{Ta} \quad (17)$$

$$\Delta\mu_O = \mu_O - \frac{1}{2}E^{gas}_{O_2} \quad (18)$$

where E^{bulk}_K and E^{bulk}_{Ta} are the calculated total energy per atom from the bulk K and Ta at their most stable low-temperature phase, and $E^{gas}_{O_2}$ is total energy of the isolated ground state O_2 molecule. By using the equations 15-18, eq. 14 can be rewritten as:

$$\omega_i = \phi_i - \frac{1}{2S}[(N_K - N_{Ta})\Delta\mu_K + (N_O - 3N_{Ta})\Delta\mu_O] \quad (19)$$

$$\phi_i = \frac{1}{2S}[(E^i_{slab} - N_{Ta}E^{bulk}_{KTaO_3}) - (N_K - N_{Ta})E^{bulk}_K - (N_O - 3N_{Ta})(\frac{E^{gas}_{O_2}}{2}) \quad (20)$$

It is worth noting that the chemical potentials strongly depend on the material growth condition. Hence, by imposing a series of thermodynamic boundary conditions,we next determined the ranges of the chemical potentials. First, the K, Ta, and O atoms are assumed to form no precipitation on the surface, then their chemical potentials must be lower than the energy of these atoms in their stable phase:

$$\Delta\mu_K < 0 \quad (21)$$

$$\Delta\mu_{Ta} < 0 \quad (22)$$

$$\Delta\mu_O < 0 \quad (23)$$

These equations define the upper boundaries of $\Delta\mu_K$, $\Delta\mu_{Ta}$ and $\Delta\mu_O$. By combining equations 15 and 22, we could obtain the following lower boundary:

$$\Delta\mu_K + 3\Delta\mu_O > \Delta H_f(KTaO_3) \quad (24)$$

with

$$\Delta H_f(KTaO_3) = E^{bulk}_{KTaO_3} - E^{bulk}_K - E^{bulk}_{Ta} - \frac{3}{2}E^{gas}_{O_2} \quad (25)$$

where $\Delta H_f(KTaO_3)$ is the formation energy of bulk $KTaO_3$, with a calculated value of -15.65 eV that is consistent with the experimental value of -14.60 eV.[63] Therefore, $\Delta\mu_K$ and $\Delta\mu_O$ can be restricted in the range of [−15.65, 0] and [−5.22, 0], respectively, with a constraint $\Delta\mu_K + 3\Delta\mu_O > -15.65$ eV.

To avoid the condensation of oxides K_2O on the $KTaO_3$ surface, the following boundary condition should be fulfilled:

$$2\Delta\mu_K + \Delta\mu_O < \Delta H_f(K_2O) \quad (26)$$

with

$$\Delta H_f(K_2O) = E^{bulk}_{K_2O} - 2E^{bulk}_K - \frac{1}{2}E^{gas}_{O_2} \quad (27)$$

in which $\Delta H_f(K_2O)$ is K_2O formation enthalpy. Similarly, to avoid the formation of Ta_2O_5, we have the boundary condition:

$$2\Delta\mu_{Ta} + 5\Delta\mu_O < \Delta H_f(Ta_2O_5) \quad (28)$$

with

$$\Delta H_f(Ta_2O_5) = E^{bulk}_{Ta_2O_5} - 2E^{bulk}_{Ta} - \frac{5}{2}E^{gas}_{O_2} \quad (29)$$

By combing equations 15 and 28, the limitation boundary for Ta_2O_5 can be written as

$$2\Delta\mu_K + \Delta\mu_O > 2\Delta H_f(KTaO_3) - \Delta H_f(Ta_2O_5) \quad (30)$$

in which $\Delta H_f(Ta_2O_5)$ is the formation enthalpy of Ta_2O_5. Then the limitation boundary can be further simplified as -7.58 eV $< 2\Delta\mu_K + \Delta\mu_O < -3.66$ eV, which corresponds to the precipitation line of Ta_2O_5 and precipitation line of K_2O, respectively. For a clean surface, the surface energy must be positive. Otherwise, the bulk solid would disintegrate, *i.e.*, to maximize its surface area. This condition can be determined by the following equation:

$$\Omega_i(\Delta\mu_K, \Delta\mu_O) > 0 \quad (31)$$

By using above boundary conditions of chemical potentials, we are able to generate the surface diagrams of the (001), (110), and (111) surfaces of $KTaO_3$, which are shown in Fig. 4, Fig. 5 and Fig. 6, respectively. In these surface phase diagrams, the stable bulk $KTaO_3$ phase is shown by the region filled with lines.

For $KTaO_3$ (001) polar surface (see Fig. 4), by using the surface grand potential condition, *i.e.*, equation 31, we can get boundary condition $\Delta\mu_K + \Delta\mu_O < -2.45$ eV for KO surface termination, and $\Delta\mu_K + \Delta\mu_O > -7.38$ eV for TaO_2 surface termination. Next, by setting $\Omega_{KO} = \Omega_{TaO_2}$, *i.e.*, the surface grand potential with KO termination equals to that with TaO_2 termination, we can get the boundary condition between the KO-terminated and TaO_2-terminated (001) surface: $\Delta\mu_K + \Delta\mu_O = -4.90$ eV. The blue-shaded area with lines in Fig. 4 shows the diagram that the KO-terminated surface is thermodynamically more stable, and the red-shaded area with lines shows the diagram that the TaO_2-terminated surface is thermodynamically more stable. Next, by imposing the thermodynamic stability condition in the bulk $KTaO_3$, we can determine the surface stability diagram of the KO-terminated and TaO_2-terminated (001) surface, *i.e.*, the overlap between the blue-shaded (red-shaded) area and the solid-line-filled region above the lower boundary, see Fig. 4. It shows that the KO-terminated surface possesses a larger area in the solid-line-filled region than the TaO_2 and K-terminated surfaces, which means that there are more space of adjusting $\Delta\mu_K$ and $\Delta\mu_O$ to obtain KO-terminated surface than the TaO_2-terminated surface. Therefore, for the $KTaO_3$ (001) surface, the KO surface termination can be considered as the most likely formed surface for further investigation. Interestingly, a very recent experimental study of the $KTaO_3$ (001) surface shows that KO planes are always on top of $KTaO_3$ (001) single crystal after cleavage,[8] which is in a good agreement with our calculations. This conclusion also coincides with an early experimental observation in which KO is shown to be dominant at the top of the surface while TaO_2 is more abundant in the deeper subsurface layers when $KTaO_3$ is heated

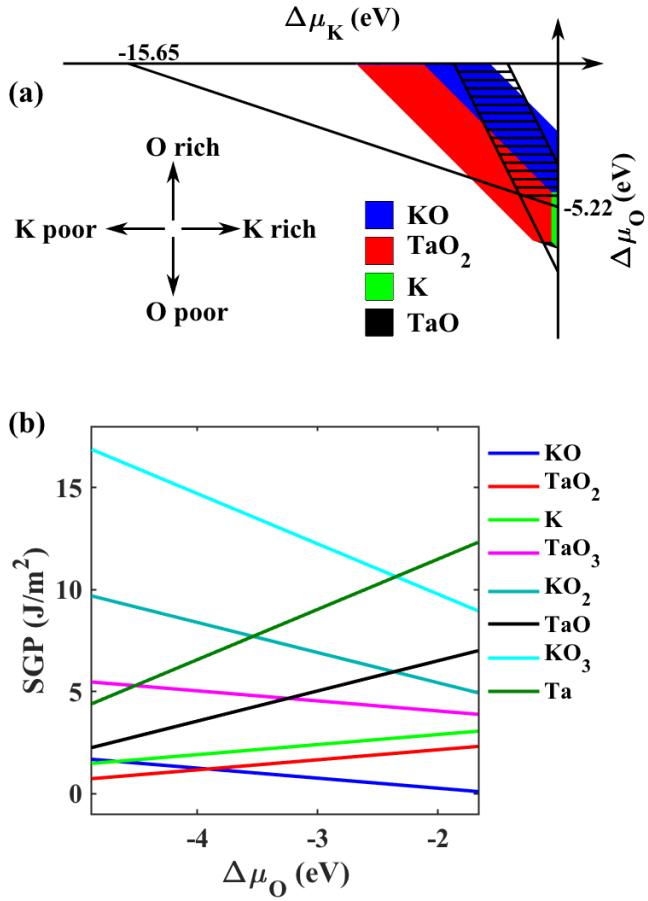

Fig. 4 (Color online)(a) Stability diagram of the (1×1) $KTaO_3$ (001) polar surface. The surface grand potentials (SGPs) are represented as a function of the $\Delta\mu_K$ and $\Delta\mu_O$ in a unit of eV. The boundary values of $\Delta\mu_K$ (-15.65) and $\Delta\mu_O$ (-5.22) are derived from the boundary of formation enthalpy of $KTaO_3$, *i.e.*, equation 24. In this and each subsequent stability diagrams, the region filled with lines indicates the allowed region for stable bulk $KTaO_3$ phase, and the shaded regions with different colors indicate the allowed region for the surface models with different terminations. In this phase diagram, the blue, red, green, and black shaded regions indicate the allowed region for KO-, TaO_2, K, and TaO-terminated surfaces, respectively. (b) The SGPs of different terminations of $KTaO_3$ (001) surface in the condition of $\Delta\mu_K = -1$ eV.

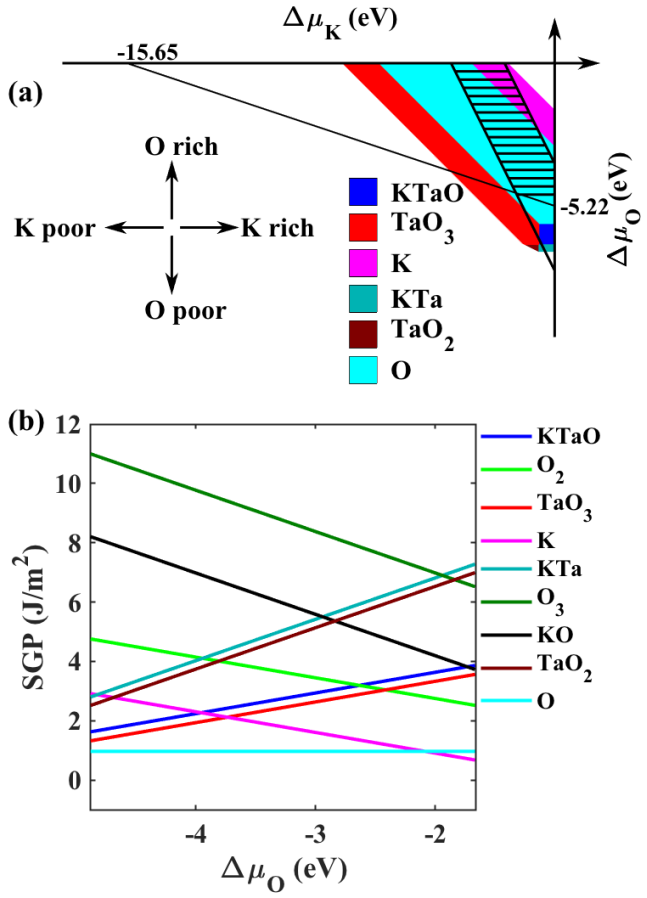

Fig. 5 (Color online) Stability diagram of the (1×1) $KTaO_3$ (110) surface. The SGPs are represented as a function of the $\Delta\mu_K$ and $\Delta\mu_O$. (b) The SGPs of different terminations of $KTaO_3$ (110) surface in the condition of $\Delta\mu_K = -1$ eV.

up to 800 °C in oxidizing conditions.[64] To show the competition between these surface terminations, we further plot their SGPs as a function of $\Delta\mu_O$ at $\Delta\mu_K = -1$ eV, see Fig. 4b. The results show that the KO termination is stable at -3.90 eV $< \Delta\mu_O < -1.66$ eV, while the TaO_2 termination is stable at $\Delta\mu_O < -3.90$ eV.

By using the same approach, we produced the surface stability diagrams for $KTaO_3$ (110) and (111) surfaces. In the case of $KTaO_3$ (110) surface, there are two types of stabilized surface terminations, *i.e.*, K, and O termination, see Fig. 5a. This is different from the case of $LaAlO_3$ system, in which there exists only one non-stoichiometric termination, *i.e.*, O termination in the thermodynamically stabilized region.[43] For $KTaO_3$ (110) surface, O termination has the largest stability domain in the O- and K-moderate condition. As $\Delta\mu_K$ and $\Delta\mu_O$ increase, the K termination turns into the thermodynamically stabilized. In short, our calculations indicate that O termination is the main surface termination for $KTaO_3$ (110) surface in reality. To clearly show the competition among these surface terminations, we present their SGPs as a function of $\Delta\mu_O$ at $\Delta\mu_K = -1$ eV in Fig. 5b. It shows that the SGP of the self-complementary O termination is a constant of 0.98 J/m^2, and has a lower SGP at a larger interval, while K terminations exist in a smaller interval in the O-rich environment.

For $KTaO_3$ (111) surface, there are eight total possible surface terminations, and only six of them can be be plotted in the surface stability diagram, see Fig. 6. This is because KO_3 and TaO_3 terminations are unstable since their SGPs are much larger than other terminations within the $\Delta\mu_O$- and $\Delta\mu_K$- allowed regions. The calculated surface stability diagram shows that only KO_2, TaO, KO and TaO_2 surface terminations are thermodynamically stabilized. The TaO_2 surface termination is stabilized within a small region; KO and TaO surface terminations dominate relatively larger regions; and KO_2 surface termination has the largest stability domain in the O-rich and K-rich environment. This indicates that the KO_2-terminated (111) surface is the most likely formed structure in reality. The SGPs of these different surface terminations as a function of $\Delta\mu_O$ at $\Delta\mu_K = -1$ eV are plotted in Fig. 6b. In this condition, only the TaO and KO_2 surface terminations can be stabilized, and TaO surface termination is more stable at $\Delta\mu_O <$

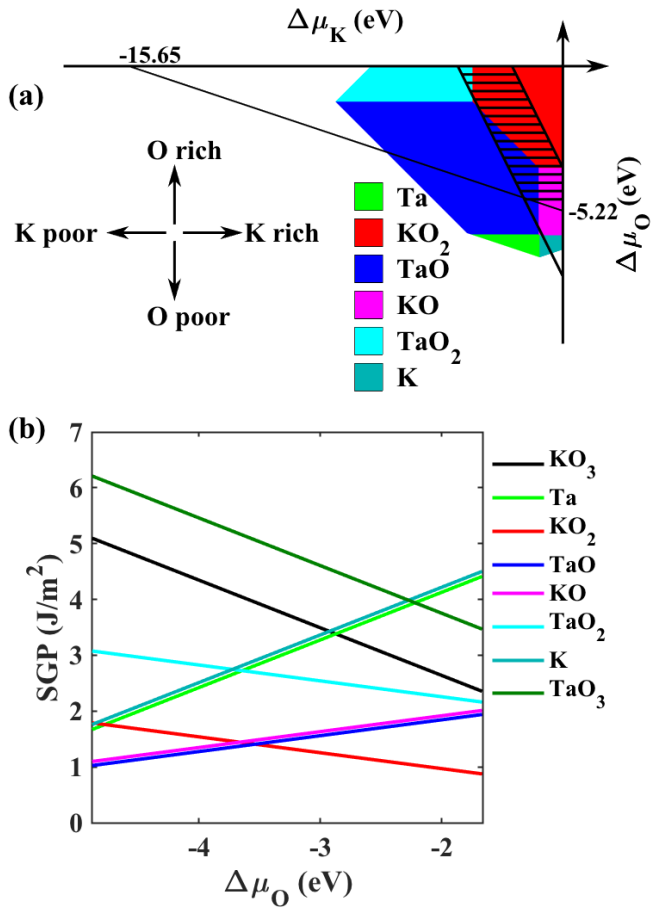

Fig. 6 (Color online) Stability diagram of the (1×1) $KTaO_3$ (111) surface. The SGPs are represented as a function of the $\Delta\mu_K$ and $\Delta\mu_O$. (b) The SGPs of different terminations of $KTaO_3$ (111) surface in the condition of $\Delta\mu_K = -1$ eV.

-3.54 eV, while KO_2 surface termination is more stable at $\Delta\mu_O > -3.54$ eV.

4 Conclusions

In summary, we have investigated the structural reconstruction, charge compensation, and thermodynamic stability of 25 types of $KTaO_3$ (001), (110), and (111) (1×1) polar surfaces using first-principles electronic structure calculations. It is found that the structural reconstruction mainly occurs in the first three outermost layers for all the surface terminations. The dipole moments of these polar surfaces are canceled out by charge redistribution on the surface layers to achieve a charge compensation, along with a surface metallization. Among these considered surface models, the (001) stoichiometric plane has the lowest cleavage energy and surface energy, while the stoichiometric KO_3/Ta (111) plane has the highest cleavage energy and the KO_3 (111) termination has the highest surface energy. The calculated phase stability diagrams with respect to the chemical potentials of component elements show that KO (001), O (110), and KO_2 (111) surface terminations possess the largest stability domain, indicating that they are more likely to be formed compared with other surface terminations. This work provides informative guidance to accurately control the surface morphology of polar perovskite oxide $KTaO_3$.

5 Acknowledgments

This work was supported by the National Science Foundation under award number ACI-1550404. JL acknowledges the Vannevar Bush Faculty Fellowship program sponsored by the Basic Research Office of the Assistant Secretary of Defense for Research and Engineering (under the Office of Naval Research grant N00014-16-1-2569). This work used the Extreme Science and Engineering Discovery Environment (XSEDE), which is supported by National Science Foundation grant number OCI-1053575. YW thanks for the financial support from the Xihua University (Z17104).

References

1 J. Mannhart and D. G. Schlom, *Science*, 2010, **327**, 1607–1611.
2 D. G. Schlom and J. Mannhart, *Nat. Mater.*, 2011, **10**, 168–169.
3 J. Chakhalian, A. J. Millis and J. Rondinelli, *Nat. Mater.*, 2012, **11**, 92–94.
4 L. Bjaalie, B. Himmetoglu, L. Weston, A. Janotti and C. G. V. de Walle, *New J. Phys.*, 2014, **16**, 025005.
5 S. Stemmer and S. James Allen, *Annu. Rev. Mater. Sci.*, 2014, **44**, 151–171.
6 K. Yang, S. Nazir, M. Behtash and J. Cheng, *Sci. Rep.*, 2016, **6**, 34667.
7 A. Ohtomo and H. Y. Hwang, *Nature*, 2004, **427**, 423–426.
8 M. Setvin, M. Reticcioli, F. Poelzleitner, J. Hulva, M. Schmid, L. A. Boatner, C. Franchini and U. Diebold, *Science*, 2018, **359**, 572–575.
9 S. Nazir, J. Cheng and K. Yang, *ACS Appl. Mater. Interfaces*, 2016, **8**, 390–399.
10 J. Cheng, S. Nazir and K. Yang, *ACS Appl. Mater. Interfaces*, 2016, **8**, 31959–31967.
11 Y. Wang, T. Wu, J. Cheng, M. Behtash and K. Yang, *ACS Appl. Mater. Interfaces*, 2016, **8**, 13659–13668.
12 P. H. Joo, M. Behtash and K. Yang, *Phys. Chem. Chem. Phys.*, 2015, **18**, 857–865.
13 J. Zhu, H. Li, L. Zhong, P. Xiao, X. Xu, X. Yang, Z. Zhao and J. Li, *ACS Catal.*, 2014, **4**, 2917–2940.
14 H. Kato, K. Asakura and A. Kudo, *J. Am. Chem. Soc.*, 2003, **125**, 3082–3089.
15 Y. Wang, W. Tang, J. Cheng, S. Nazir and K. Yang, *Phys. Chem. Chem. Phys.*, 2016, **18**, 31924–31929.
16 J. Cheng, J. Luo and K. Yang, *ACS Appl. Mater. Interfaces*, 2017, **9**, 7682–7690.
17 F. Wang, Z. Ren, H. Tian, S. A. Yang, Y. Xie, Y. Lu, J. Jiang, G. Han and K. Yang, *ACS Appl. Mater. Interfaces*, 2017, **9**, 1899–1906.
18 Y. Lu, F. Wang, M. Chen, Z. Lan, Z. Ren, H. Tian and K. Yang, *ACS Appl. Mater. Interfaces*, 2018, **10**, 10536–10542.
19 A. F. Santander-Syro, C. Bareille, F. Fortuna, O. Copie, M. Gabay, F. Bertran, A. Taleb-Ibrahimi, P. Le Fèvre, G. Her-

ranz, N. Reyren, M. Bibes, A. Barthélémy, P. Lecoeur, J. Guevara and M. J. Rozenberg, *Phys. Rev. B*, 2012, **86**, 121107.
20 P. D. C. King, R. H. He, T. Eknapakul, P. Buaphet, S.-K. Mo, Y. Kaneko, S. Harashima, Y. Hikita, M. S. Bahramy, C. Bell, Z. Hussain, Y. Tokura, Z.-X. Shen, H. Y. Hwang, F. Baumberger and W. Meevasana, *Phys. Rev. Lett.*, 2012, **108**, 117602.
21 C. Bareille, F. Fortuna, T. C. Rodel, F. Bertran, M. Gabay, O. H. Cubelos, A. Taleb-Ibrahimi, P. L. Fevre, M. Bibes, A. Barthelemy, T. Maroutian, P. Lecoeur, M. J. Rozenberg and A. F. Santander-Syro1, *Sci. Rep.*, 2014, **4**, 3584.
22 K. Ueno, S. Nakamura, H. Shimotani, H. T. Yuan, N. Kimura, T. Nojima, H. Aoki, Y. Iwasa and M. Kawasaki, *Nat. Nanotechnol.*, 2011, **6**, 408–412.
23 K. Shanavas, *J Electron Spectrosc.*, 2015, **201**, 121–126.
24 H. Nakamura and T. Kimura, *Phys. Rev. B*, 2009, **80**, 121308.
25 K. V. Shanavas and S. Satpathy, *Phys. Rev. Lett.*, 2014, **112**, 086802.
26 C. Noguera, *J. Phys.: Condens. Matter*, 2000, **12**, R367.
27 S. Harashima, C. Bell, M. Kim, T. Yajima, Y. Hikita and H. Y. Hwang, *Phys. Rev. B*, 2013, **88**, 085102.
28 J. Kubacki, A. Molak, M. Rogala, C. Rodenbücher and K. Szot, *Surf. Sci.*, 2012, **606**, 1252–1262.
29 D. E. E. Deacon-Smith, D. O. Scanlon, C. R. A. Catlow, A. A. Sokol and S. M. Woodley, *Adv. Mater.*, 2014, **26**, 7252–7256.
30 G. Kresse and J. Furthmüller, *Phys. Rev. B*, 1996, **54**, 11169–11186.
31 G. Kresse and D. Joubert, *Phys. Rev. B*, 1999, **59**, 1758–1775.
32 P. E. Blöchl, *Phys. Rev. B*, 1994, **50**, 17953–17979.
33 J. P. Perdew, K. Burke and M. Ernzerhof, *Phys. Rev. Lett.*, 1996, **77**, 3865–3868.
34 E. Sanville, S. D. Kenny, R. Smith and G. Henkelman, *J. Comput. Chem.*, 2007, **28**, 899–908.
35 W. Tang, E. Sanville and G. Henkelman, *J. Phys.: Condens. Matter*, 2009, **21**, 084204.
36 S. H. Wemple, *Phys. Rev.*, 1965, **137**, A1575.
37 D. J. Singh, *Phys. Rev. B*, 1996, **53**, 176.
38 J. Neugebauer and M. Scheffler, *Phys. Rev. B*, 1992, **46**, 16067–16080.
39 P. W. Tasker, *J. Phys. C: Solid State Phys.*, 1979, **12**, 4977.
40 C. Noguera, A. Pojani, F. Finocchi and J. Goniakowski, in *Stability of Polar Oxide Surfaces*, 1997, pp. 455–478.
41 C. Noguera, A. Pojani, P. Casek and F. Finocchi, *Surf. Sci.*, 2002, **507**, 245–255.
42 F. Bottin, F. Finocchi and C. Noguera, *Phys. Rev. B*, 2003, **68**, 035418.
43 H. Chen, Y. hong Ding, H. tao Yu and Y. Xie, *J. Phys. Chem. C*, 2015, **119**, 9364–9374.
44 H. Chen, Y. Xie, G.-X. Zhang and H.-T. Yu, *J. Phys.: Condens. Matter*, 2014, **26**, 395002.
45 F. Bottin, F. Finocchi and C. Noguera, *Phys. Rev. B*, 2003, **68**, 035418.
46 G.-X. Zhang, Y. Xie, H.-T. Yu and H.-G. Fu, *J. Comput. Chem.*, 2009, **30**, 1785–1798.
47 Y. Xie, H. tao Yu, G. xu Zhang, H. gang Fu, and J. zhong Sun, *J. Phys. Chem. C*, 2007, **111**, 6343–6349.
48 E. Heifets, J. Ho and B. Merinov, *Phys. Rev. B*, 2007, **75**, 155431.
49 Y. Yin, J. Wang, H. Zhu, K. Lv and X. Wu, *Vacuum*, 2015, **120**, 83–88.
50 R. I. Eglitis and M. Rohlfing, *J. Phys.: Condens. Matter*, 2010, **22**, 415901.
51 P. R. Cantwell, M. Tang, S. J. Dillon, J. Luo, G. S. Rohrer and M. P. Harmer, *Acta Mater.*, 2014, **62**, 1–48.
52 W. D. Kaplan, D. Chatain, P. Wynblatt and W. C. Carter, *J. Mater. Sci.*, 2013, **48**, 5681–5717.
53 S. A. E. Johansson and G. Wahnstrom, *Phys. Rev. B*, 2012, **86**, 035403.
54 N. Zhou and J. Luo, *Acta Mater.*, 2015, **91**, 202–216.
55 J. Luo, *J. Am. Ceram. Soc.*, 2012, **95**, 2358–2371.
56 X. Shi and J. Luo, *Phys. Rev. B*, 2011, **84**, 014105.
57 J. Luo, *Curr. Opin. Solid State Mater. Sci.*, 2008, **12**, 81–88.
58 M. Tang, W. C. Carter and R. M. Cannon, *Phys. Rev. Lett.*, 2006, **97**, 075502.
59 M. Tang, W. C. Carter and R. M. Cannon, *Phys. Rev. B*, 2006, **73**, 024102.
60 Y. Mishin, W. Boettinger, J. Warren and G. McFadden, *Acta Mater.*, 2009, **57**, 3771–3785.
61 P. Wynblatt and D. Chatain, *Mater. Sci. Eng. A*, 2008, **495**, 119–125.
62 A. Pojani, F. Finocchi and C. Noguera, *Surf. Sci.*, 1999, **442**, 179–198.
63 S. K. Sahu, S. Zlotnik, A. Navrotsky and P. M. Vilarinho, *J. Mater. Chem. C*, 2015, **3**, 7691–7698.
64 V. V. Laguta, M. D. Glinchuk, I. P. Bykov, L. J. J. Rosa, M. Savinov, and Z. Trybula, *Phys. Rev. B*, 2000, **61**, 3897.